



Experimental identification of high order Lamb waves and estimation of the mechanical properties of a dry human skull

Matteo Mazzotti^{a,*}, Christopher Sugino^b, Eetu Kohtanen^b, Alper Erturk^b, Massimo Ruzzene^a

^a P.M. Rady Department of Mechanical Engineering, University of Colorado Boulder, Boulder, USA

^b G.W. Woodruff School of Mechanical Engineering, Georgia Institute of Technology, Atlanta, USA

ARTICLE INFO

Keywords:

Cranial Lamb waves
Human skull
Dispersion
Orthotropy
Parametric identification
Semi-analytical finite element method

ABSTRACT

We experimentally investigate and characterize high order Lamb wave modes in a dry human skull. Specifically, we show that the diploë supports distinct wave modes in the sub-1.0 MHz frequency regime, and we employ these modes for the estimation of equivalent mechanical properties of cortical and trabecular bones. These modes are efficiently generated in a parietal region by direct contact excitation with a wedge beam transducer, and are recorded via infrared laser vibrometry. Frequency/wavenumber data are estimated using a matrix pencil method applied to wavefield measurements recorded on the outer cortical surface. The semi-analytical finite element model of an equivalent three-layered plate provides the platform for the identification of wave modes based on their through-the-thickness profiles, and supports the estimation of equivalent mechanical properties in conjunction with an optimization algorithm developed for this purpose. The results presented herein illustrate how high order Lamb waves can be used to gain understanding of the wave properties of a human skull and to estimate the orthotropic and equivalent isotropic mechanical properties of cortical and trabecular bones.

1. Introduction

Recently, guided ultrasonic waves (GUWs) have emerged as a viable tool to complement transcranial focused ultrasound (tFUS) for brain imaging and therapy, especially at the brain periphery or skull-brain interface [1]. While tFUS applications are inherently limited to central regions of the brain and suffer from major drawbacks such as bone heating and inefficient transmission [2–7], GUWs can exploit the waveguide-like nature of the cranial bone to efficiently focus ultrasound waves into the brain by mode conversion [1]. Moreover, the ability of GUWs to carry mechanical energy for long distances may be considered for the inspection of different areas of the cranial vault or to reach both the near and far field regions of the brain. Thus, effective employment of GUWs may increase the medical possibilities offered by ultrasound imaging and possibly create new treatment options for a variety of neurological conditions.

Guided waves are highly dispersive [8–13], with a nonlinear frequency-wavenumber relation for each of the infinite number of modes supported by the waveguide. Thus, the effective use of GUWs for imaging and/or material characterization strongly relies on the *a priori* knowledge of the dispersion properties of the medium under

consideration. In recent years, different studies have investigated the dispersion properties of long [14–16] and cranial [17–21] bones. Near-field guided waves have been first experimentally observed by Estrada et al. in rodent [22,23,20] and human [19,20] skulls. In these works, water-immersed skull samples were excited with short laser pulses on their outer surface, while their near-field optoacoustically-induced response was measured using needle hydrophones that closely map the skull's inner surface. The experimental near-field dispersion diagrams were then interpreted with the aid of multi-layered plate waveguide models, which were used to determine the corresponding numerical Lamb wave dispersion spectra. By using the above methodology, it was demonstrated that quasi-Rayleigh guided modes can propagate within the cortical tables of a human skull in the 0.2–1.5 MHz regime [19]. However, although high order modes were also excited in the skull sample, their individual identification was made difficult by experimental setup limitations and by the strong scattering occurring within the diploë. These limitations suggest that such effects still need to be explored. A different approach was presented in Adams et al. [17,18], where the group velocity dispersion curves of leaky Lamb modes were numerically computed in a water-immersed skull by means of a concave phased array transducer. Using a three-layered cylindrical waveguide as

* Corresponding author.

E-mail address: teomazzotti@gmail.com (M. Mazzotti).

<https://doi.org/10.1016/j.ultras.2020.106343>

Received 8 September 2020; Received in revised form 9 November 2020; Accepted 23 December 2020

Available online 16 January 2021

0041-624X/© 2021 Elsevier B.V. All rights reserved.

supporting mathematical model, the authors demonstrated numerically that the concave array setup could be used to generate and detect several flexural modes. More recently, experimental and numerical investigations of guided waves in a 3D-printed bone phantom generated from CT scan images of a human skull were presented in Gao et al. [21]. Although high order Lamb modes were observed, the bone phantom did not include the diploë and the materials were limited to homogeneous isotropic polymers.

To the best of our knowledge, experimental detection of distinct high order cranial Lamb modes and their characterization still offers numerous opportunities to improve the understanding of wave motion in the skull, and to explore potential opportunities offered in terms of mechanical characterization and the potential development of imaging tools. For example, generating and controlling high order guided waves in the skull can provide fundamental insights on the dynamic behavior of the diploë in different frequency regimes. To fill existing gaps, this work aims at developing experimental and numerical procedures for the identification of high order Lamb wave modes in the human skull. High order cranial Lamb waves are investigated in the upper parietal region of a dry human skull by means of ultrasonic tests and semi-analytical finite element (SAFE) analyses. The experimental dispersion spectrum of the parietal region is retrieved from time-velocity arrays recorded with an infrared scanning laser Doppler vibrometer and analyzed with a matrix pencil method. The different high order Lamb modes in the spectrum are then identified by matching the corresponding dispersion curves with those obtained from the SAFE model. In addition, the mechanical properties of the parietal bone are identified as part of a numerical-to-experimental mode matching process.

2. Methods

2.1. Experimental setup

The study is conducted on the upper left parietal region of a dry human skull specimen from a 49-year old Caucasian male of unknown medical history. The geometry of the skull was captured through computerized tomography (CT) scan in order to inform models developed as part of this work. CT scans with 0.625 mm coronal sections were performed using the Philips Gemini 64TF imaging system of the CU Anschutz C-TRIC PET/CT Imaging Center (USA). The reconstructed CT-scanned model of the specimen is shown in Fig. 1(a) along with the investigated parietal region. The latter corresponds to a square surface

of 41 mm × 41 mm side length and does not include any major diploic channel, as can be noted from the coronal and sagittal sections of Fig. 1 (b) and (c), respectively.

To obtain velocity time histories at different locations of the investigated parietal region, the skull was instrumented with an angle beam transducer (Olympus C543-SM, 5 MHz, 0.25 in) mounted on a 60° wedge as indicated in Fig. 2. The wedge location and orientation was selected to allow the propagation of Lamb waves away from the temporal region, where the overall thickness undergoes large variations and the diploë is almost absent (Fig. 1(b)). Lamb waves were generated in the parietal bone by means of a 2.5 cycle toneburst centered at 500 kHz. The corresponding 3D velocity array $A(x, y, t)$ was recorded on a regular grid of 0.3106 mm with a Polytec PSV-500 Xtra infrared scanning laser Doppler Vibrometer (SLDV). At each point of the measurement grid, velocity waveforms of 1.60 ms duration were acquired at a sampling frequency of $s_f = 3.125$ MHz with a 500 Hz repetition rate and 2% pre-triggering. A snapshot of the velocity field recorded at the time instant $t = 51.2 \mu\text{s}$ can be observed in Fig. 2. From the surface velocity measurement, the interpolated dashed line in Fig. 2 was found to show the best signal-to-noise ratio (SNR) and its corresponding velocity array $v(t_n, s_m)$, shown in Fig. 3(a), was used for the dispersion analysis discussed in the remainder of this work. In this array, $t_n = (n-1)/s_f$, ($n = 1, \dots, N = 5000$), defines the n -th time sample while $s_m = (m-1)\Delta s$, ($m = 1, \dots, M = 150$), indicates the m -th interpolated spatial location along the line scan, in which $\Delta s = 0.2879$ mm corresponds to the spatial step between interpolated points along the line. The frequency-wavenumber ($f - \kappa$) spectrum of the array, indicated with $\hat{v}(f, \kappa)$ and obtained from a 2D fast Fourier transform (2DFFT) of $v(t, s)$, is shown in Fig. 3(b). The extraction of the different dispersion branches in this spectrum is described in detail in the next section.

2.2. Dispersion curves using the matrix pencil method

The frequency-wavenumber dispersion curves of an expected number of Lamb modes Q in the array $v(t_n, s_m)$ are retrieved with a modified matrix pencil method (MPM) [24–26]. This method allows the direct evaluation of the complex wavenumbers $\kappa(f_0)$ at a given frequency f_0 while simultaneously suppressing noise effects. The first step of the method consists in forming the Hankel matrix

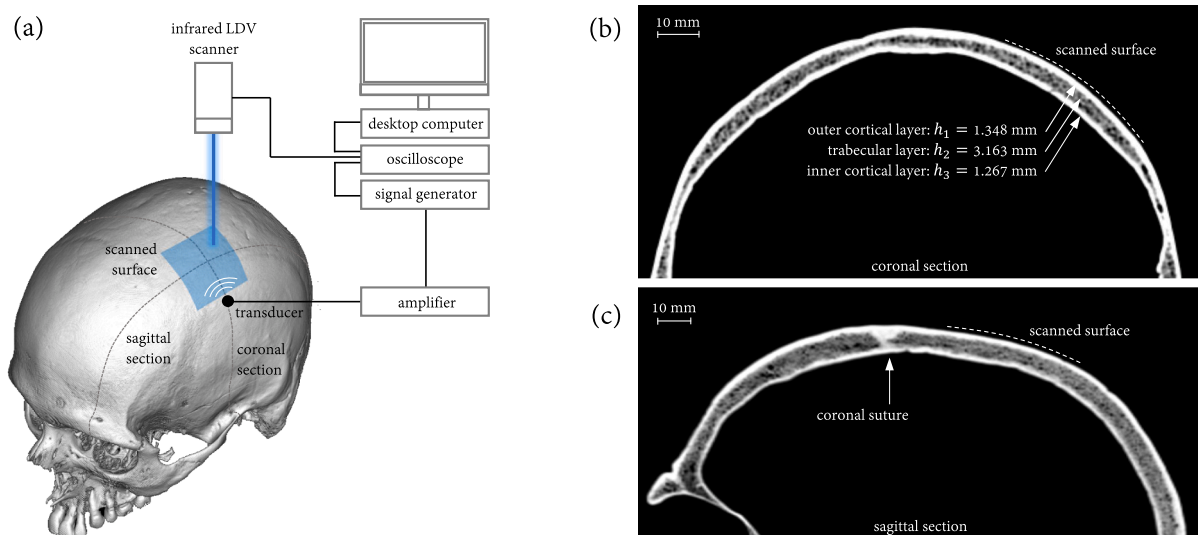


Fig. 1. (a) Schematic of the experimental setup showing the CT-scanned 3D model of the dry skull with coronal and sagittal sections. (b) Coronal section with scanned surface and average thickness of outer cortical, trabecular and inner cortical layers. (c) Sagittal section with scanned surface.

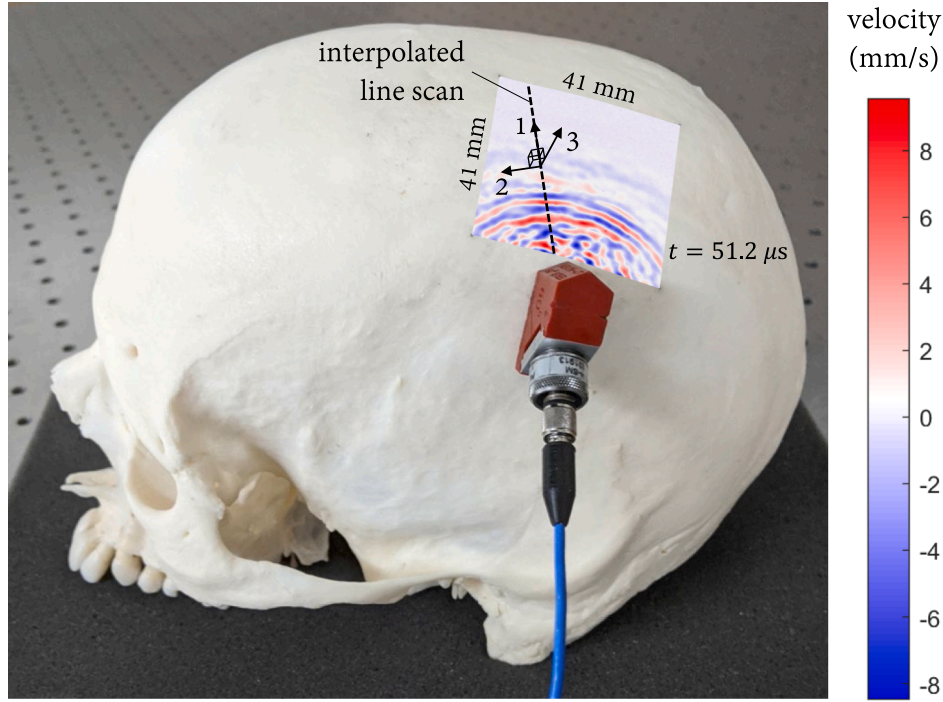


Fig. 2. Snapshot of the surface velocity field recorded with the infrared scanning laser Doppler Vibrometer at time $t = 51.2 \mu\text{s}$ and interpolated line scan used in the analysis of Section 2.2. The local frame of reference 123 is used in the definition of the orthotropic material properties of Table 1 and the displacement profiles of Fig. 4(b).

$$\mathbf{X}(f_0) = \begin{bmatrix} \hat{v}(f_0, s_1) & \dots & \hat{v}(f_0, s_{P+1}) \\ \hat{v}(f_0, s_2) & \dots & \hat{v}(f_0, s_{P+2}) \\ \vdots & \ddots & \vdots \\ \hat{v}(f_0, s_{M-P}) & \dots & \hat{v}(f_0, s_M) \end{bmatrix}, \quad (1)$$

where P is the pencil parameter satisfying the condition $Q \leq P \leq M - Q$, and $\hat{v}(f_0, s_m)$ is the time Fourier transform of $A(t, s_m)$ evaluated at the location s_m and frequency f_0 . In this work, the optimal value of the pencil parameter was found to be $P = 40$. Such value was determined in an iterative fashion by performing several analyses in the range $P \in [20, 100]$. To improve the SNR in $\mathbf{X}(f_0)$, the singular value decomposition (SVD) $\mathbf{X} = \mathbf{U}\mathbf{\Sigma}\mathbf{V}^H$ [27] is performed, where \mathbf{U} and \mathbf{V} are complex unitary matrices and $\mathbf{\Sigma} = \text{diag}(\sigma_1, \sigma_2, \dots)$ is a diagonal matrix containing the non-negative singular values of \mathbf{X} in descending order. By performing a rank test and retaining only the first R dominant singular values of $\mathbf{X}(f_0)$, two rank-reduced matrices are reconstructed from the parent Hankel matrix as $\mathbf{X}_1(f_0) = \mathbf{U}\mathbf{\Sigma}_1\mathbf{V}_1^H$ and $\mathbf{X}_2(f_0) = \mathbf{U}\mathbf{\Sigma}_2\mathbf{V}_2^H$, where $\mathbf{\Sigma}_1 = \text{diag}(\sigma_1, \dots, \sigma_R)$, $\mathbf{V}_1 = \mathbf{V}(2:P+1, 1:R)$ and $\mathbf{V}_2 = \mathbf{V}(1:P, 1:R)$. To compute the spatial wavenumbers $\kappa(f_0)$, a set of backward exponential estimates $\lambda_r^<$ ($r = 1, \dots, R$) and forward exponential estimates $\lambda_r^>$ are first obtained from the two eigenvalue problems

$$(\mathbf{X}_1^+ \mathbf{X}_2 - \lambda_r^< \mathbf{I}) \mathbf{e}_r^< = \mathbf{0}, \quad (\mathbf{X}_1^+ \mathbf{X}_2 - \lambda_r^> \mathbf{I}) \mathbf{e}_r^> = \mathbf{0}, \quad (2)$$

where $(\cdot)^+$ indicates the Moore–Penrose generalized inverse, \mathbf{I} denotes the identity matrix, and the eigenvectors $\mathbf{e}_r^<$ and $\mathbf{e}_r^>$ contain the wave amplitude at the different spatial locations. From the eigensolutions of Eq. (2), two sets of backward and forward complex wavenumbers are computed as $\kappa_r^<(f_0) = -\ln \lambda_r^< / (i\Delta s)$ and $\kappa_r^>(f_0) = \ln \lambda_r^> / (i\Delta s)$, respectively. The r th Lamb wavenumber $\kappa_r(f_0)$ is retained from the backward and forward sets if $(|\kappa_r^<(f_0)| - |\kappa_r^>(f_0)|) / |\kappa_r^>(f_0)| \leq \text{tol}_r$, where tol_r indicates the residual tolerance (here assumed equal to 0.001). The full frequency-wavenumber dispersion diagram of the array $v(t_n, s_m)$ is finally obtained from the application of the described procedure at several discrete frequencies in the high-energy frequency spectrum of the applied

toneburst, i.e. $f_0 \in [200 \text{ kHz}, 800 \text{ kHz}]$.

2.3. Mode matching using the semi-analytical finite element method

Numerical modeling is conducted in order to identify each mode in the experimental dispersion spectrum based on their thickness displacement profile. Such information is useful in establishing whether or not the different Lamb modes are mainly confined within the cortical tables (as observed in [19]) and, consequently, to determine the role of the diploë in supporting guided wave motion in various frequency regimes.

The task of classifying the observed experimental Lamb modes was carried out by numerically modeling the parietal bone as a three-layered flat plate and calculating its dispersion characteristics with the semi-analytical finite element (SAFE) method developed in [11]. The through-thickness profile of each experimental Lamb mode was then estimated by matching it with its numerical counterpart. The general form of the SAFE dispersion equation is

$$\{\kappa^2 \mathbf{K}_3(h, \mathbf{p}) + i\kappa \mathbf{K}_2(h, \mathbf{p}) + \mathbf{K}_1(h, \mathbf{p}) - \omega^2 \mathbf{M}(h, \mathbf{p})\} \mathbf{Q} = \mathbf{0}, \quad (3)$$

where $\omega = 2\pi f$ is the angular frequency, while $\mathbf{M}(h)$ and $\mathbf{K}_i(h, \mathbf{p})$ ($i = 1, 2, 3$) are mass and stiffness operators calculated as in [11]. Also, \mathbf{p} indicates a set of material parameters for the layered plate waveguide, and $h = \sum_{i=1}^3 h_i$ denotes its total thickness, where h_i is the thickness of the i -th layer. The values of h_i were determined from the coronal CT scan section of Fig. 1(b) by averaging the distances between the external cortical surfaces and the internal trabecular-cortical interfaces. The averaging was performed over a minimum of ten different locations spanning the scanned region. This resulted in an average thickness $h_1 = 1.348 \text{ mm}$ for the outer cortical table, $h_2 = 3.163 \text{ mm}$ for the diploë and $h_3 = 1.267 \text{ mm}$ for the inner cortical table.

2.4. Material properties identification

The mechanical properties were found as part of the mode identification procedure. Following the study in [28], the outer and inner

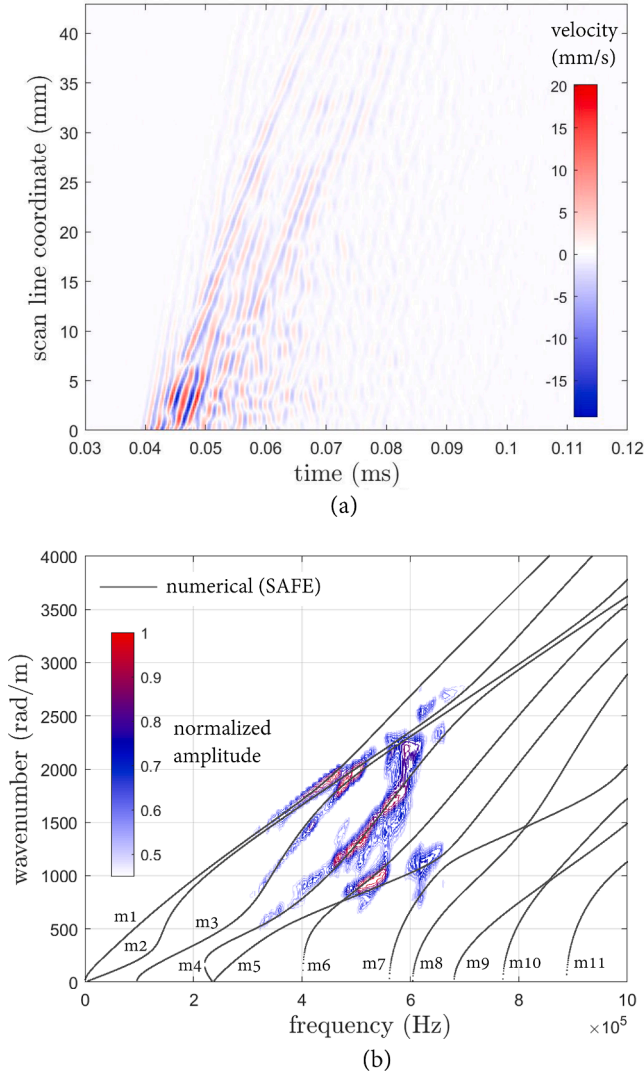


Fig. 3. (a) Surface velocity array $v(t,s)$ for the scan line of Fig. 2 and (b) corresponding 2D FFT spectrum $\hat{v}(f,k)$ with superimposed numerical dispersion curves.

cortical tables were assumed to have identical elastic orthotropic properties, while an equivalent isotropic behavior was assumed for the diploë. The full set of mechanical parameters is denoted as $\mathbf{p} = \mathbf{a} \cdot \mathbf{m}$. In this set, $\mathbf{m} = \{\mathbf{m}_c, \mathbf{m}_d\}^T$ collects the nominal density and elastic parameters (Young's modulus, shear modulus and Poisson's ratio) for the cortical tables in the vector $\mathbf{m}_c = \{\rho, E_1, E_2, E_3, G_{13}, \nu_{12}, \nu_{13}, \nu_{23}\}^T \in \mathbb{R}^8$ and for the diploë in the vector $\mathbf{m}_d = \{\rho, E, \nu\}^T \in \mathbb{R}^3$, while $\mathbf{a} = \{a_1, a_2, \dots, a_{11}\}^T, a_i \in [0, 1]$, denotes a vector of unknown $N_a = 11$ unitary coefficients used to scale the nominal values \mathbf{m} . The subscripts 1, 2 and 3 for the orthotropic material properties in \mathbf{m}_c refer to the local frame of reference defined on the interpolated scan line as shown in Fig. 2.

The set of coefficients \mathbf{a} that realizes the best fit between the numerical and experimental dispersion curves was obtained from the application of the multiplicative regularized Gauss–Newton method described in [29]. This method reconstructs \mathbf{a} as an iterative sequence $\mathbf{a}_{k+1} = \mathbf{a}_k + \delta \mathbf{a}_k$ until a convergence criteria is met. At the k -th iteration, the update $\delta \mathbf{a}_k$ is computed from the constrained trust region quadratic problem

$$\min_{\delta \mathbf{a}_k \in \mathbb{R}_{[0,1]}^{N_a} - \{\mathbf{0}\}} \left\{ (\nabla_{\mathbf{a}} \mathcal{F}(\mathbf{a}_k))^T \delta \mathbf{a}_k + \frac{1}{2} \delta \mathbf{a}_k^T \nabla_{\mathbf{a}}^2 \mathcal{F}(\mathbf{a}_k) \delta \mathbf{a}_k \right\}, \quad (4)$$

$$\text{subjected to } \mathbf{l} - \mathbf{a}_k \leq \delta \mathbf{a}_k \leq \mathbf{u} - \mathbf{a}_k,$$

$$\text{and the trust region constraint } \|\delta \mathbf{a}_k\|_{\infty} \leq \Delta_k,$$

where \mathbf{l} and \mathbf{u} denote physically admissible lower and upper bounds for the material parameters, Δ_k indicates the maximum size of the trust region hyperbox in $\mathbb{R}_{[0,1]}^{N_a}$ and

$$\mathcal{F}(\mathbf{a}_k) = N_{\omega}^{-1} \|\mathbf{r}(\mathbf{a}_k)\|_2^2 (N_a^{-1} \Delta_{k-1}^{-1} \|(\mathbf{a}_k - \mathbf{a}_{k-1})\|_2^2 + 1), \quad (5)$$

is a multiplicative regularized functional in which

$$\mathbf{r}(\mathbf{a}_k) = \left\{ \dots, \frac{\omega_i^2(\mathbf{a}_k, \kappa_j)}{\tilde{\omega}_i^2(\kappa_j)} - 1, \dots \right\}^T \quad (6)$$

represents the data misfit to be minimized. In Eq. (6), $\tilde{\omega}_i^2(\kappa)$ ($i = 1, \dots, N_{\omega}$) indicates the angular frequency of the i -th experimental Lamb mode evaluated at κ while $\omega_i(\mathbf{a}_k, \kappa)$ denotes its corresponding numerical counterpart obtained from Eq. (3) and solving the corresponding eigenvalue problem for the current solution $\mathbf{p}(\mathbf{a}_k) = \mathbf{a}_k \cdot \mathbf{m}$. Additional details on the calculation of Δ_k as well as the gradient $\nabla_{\mathbf{a}} \mathcal{F}(\mathbf{a}_k)$ and Hessian $\nabla_{\mathbf{a}}^2 \mathcal{F}(\mathbf{a}_k)$ can be found in A and [29]. Once the optimal set \mathbf{a}^* has been computed from Eq. (4), the full dispersion curves and corresponding displacement profiles are respectively obtained as the eigen-solutions $\{\kappa(\omega, \mathbf{p}(\mathbf{a}^*)), \mathbf{Q}(\omega, \mathbf{p}(\mathbf{a}^*))\}$ of Eq. (3) for any given ω . These solutions can be used to classify the different Lamb modes in the experimental dispersion spectrum, as discussed in the next section.

3. Results and discussion

The numerical dispersion curves obtained from the SAFE analysis are superimposed to the 2D FFT spectrum of the interpolated scan line in Fig. 3(b) and to the MPM results in Fig. 4(a). The numerically estimated dispersion curves for the three-layered flat plate modes agree well with the experimental ones. The latter indicate the presence of six distinct Lamb modes, which have been labeled as m_1, m_2, m_3, m_4, m_5 and m_8 . The through-thickness profiles of the in-plane and out-of-plane displacement components (corresponding to the directions 1 and 3 of the local frame of reference of Fig. 2) for these modes are shown in Fig. 4(b). The clearly discernible dispersion branches of modes m_3, m_4, m_5 and m_8 illustrate that the diploë supports high order modes characterized by more than one through-thickness wavelength. This is one of the key results of this study. This is particularly evident for modes m_4, m_5 and m_6 . It is also interesting to note that, similar to the observations in homogeneous plates, the modes m_2, m_3, m_4, m_5 and m_8 possess properties of quasi-symmetry and antisymmetry in terms of displacement distribution with respect to the center of the diploë. Although not shown in Fig. 4(b), this property was also verified for the mode m_1 outside the 200–400 kHz frequency range. Within this range, however, the quasi-symmetric properties are lost. The results of Fig. 4(a) indicate that, in the investigated frequency range, high order Lamb modes can be generated in the whole cranial bone section via direct-contact excitation.

The cranial bone material properties identified using the experimental high order Lamb modes and the analysis of Section 2.4 are listed in Table 1. Of particular interest are the values obtained for the cortical layers, which show $E_1 \approx E_2$ and $\nu_{13} \approx \nu_{23}$. These values reveal a marked transversely isotropic behavior, and confirm the observations in [28], where cortical bone samples were tested using ultrasound transmissibility techniques. For comparison, the orthotropic material parameters of the parietal region P2 in [28], which approximately correspond to the parietal region investigated in this work, have also been reported in Table 1. This comparison highlights lower values of the identified density and Young's modulus and higher values of the

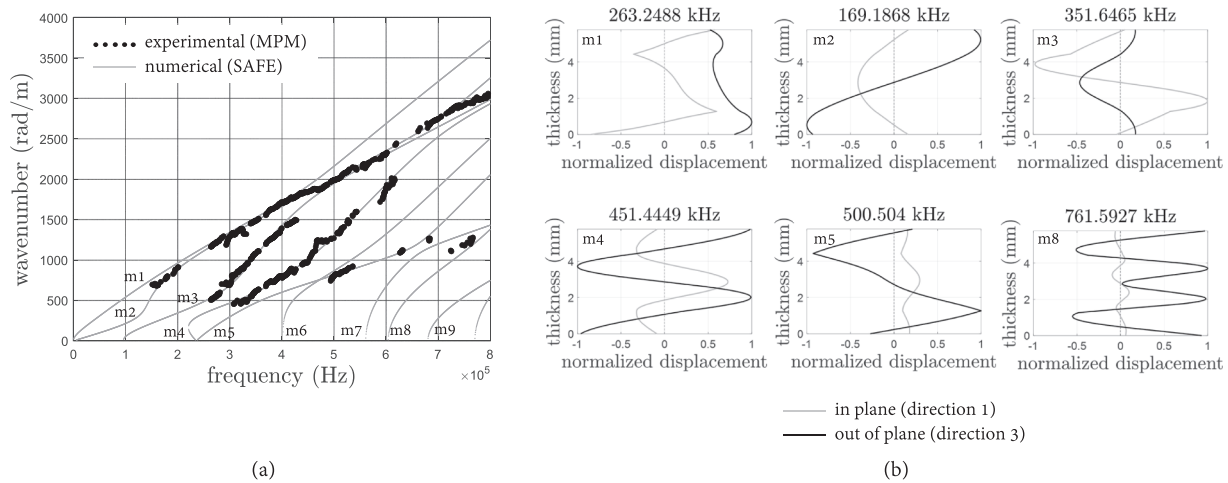


Fig. 4. (a) Experimental (MPM) versus numerical (SAFE) dispersion curves and (b) through-thickness displacement profiles for the identified Lamb modes at different frequencies. The directions 1 (in plane) and 3 (out of plane) coincide with those of Fig. 2.

Table 1
Identified mechanical parameters for the cortical and trabecular layers and comparison with data available in literature.

Layer	Reference	ρ (kg/m ³)	E_1 (GPa)	E_2 (GPa)	E_3 (GPa)	G_{13} (GPa)	ν_{12}	ν_{13}	ν_{23}
Cortical (orthotropic)	present (dry)	1569	13.50	13.29	11.57	5.71	0.617	0.479	0.465
	[28], location P2 (degassed)	1845	20.00	15.40	13.90	5.10	0.300	0.250	0.230
Trabecular (isotropic)	present (dry)	903	4.24	4.24	4.24	1.52	0.396	0.396	0.396
	[19,30] (dry)	1055	2.00	2.00	2.00	0.72	0.380	0.380	0.380

Poisson’s ratio for the investigated dry skull with respect to the average values calculated for the region P2 on 15 different skulls in [28]. Besides individual specimen-related variations, these differences may be associated to the degassing procedure used in [28]. The degassing procedure is not expected to cause significant changes in shear modulus G_{13} between a dry and degassed skull, which is confirmed by the similar values listed in Table 1. The identified mechanical parameters for the diploë indicate a slightly lower density and a higher Young’s modulus when compared to those in [19,30], whereas the Poisson’s ratio is approximately the same (see Table 1). These results may be associated to the large ranges of variation previously observed in the compressive strength of the parietal diploë [31]. Another possible cause is a stiffening effect induced by the two cortical tables [32,33].

Overall, the results discussed in this Section may potentially open new venues in GUW-based characterization of the cranial bone and marrow. In addition, procedures similar to that presented in this work have already been successfully applied to the characterization of long bones in presence of soft tissue [14–16]. From a physical standpoint, the inclusion of an external coupling medium (such as water) and a soft tissue layer in the waveguide model of the cranial bone is expected to result in additional Lamb wave modes due to the effects of increased thickness, acoustic impedance mismatch and energy radiation. Such effects could potentially be investigated in water loaded setups by means of contact [34] and non-contact excitation [19], as well as in clinical settings by contact ultrasonic transducer arrays [14].

4. Conclusions

This work demonstrates that high order guided wave modes can be effectively generated and recorded in the upper parietal region of a dry human skull. The modes can be employed to identify the orthotropic and equivalent isotropic material properties of the cortical tables and diploë, respectively. This is illustrated by extracting dispersion spectra for

cranial Lamb waves, which are analyzed by means of a matrix pencil method. The experimental dispersion curves were classified by conducting comparisons with the modes predicted in a three-layered plate waveguide, whereby thicknesses are estimated from CT scan images, while their material properties are reconstructed through a semi-analytical finite element (SAFE) model coupled with a regularized Gauss–Newton algorithm. In the computed dispersion spectrum, high order modes can be clearly detected at frequencies lower than 800 kHz. These modes are observed to possess properties of quasi-symmetry and antisymmetry with respect to the mid thickness, which is consistent with the behavior of a plate-like structure. These results indicate that, in the low and mid frequency regime, the diploë can effectively sustain a guided wave motion. In agreement with previously published studies, the identified material properties also indicate that the cortical tables behave as a transversely isotropic material. Potential implications of the obtained results include the possibility of using GUWs for the non-invasive inspection of the cranial marrow by leveraging Lamb modes with high sensitivity to small changes on the marrow’s acoustic impedance. Furthermore, GUWs could potentially be employed in conjunction with tomographic reconstruction algorithms for the imaging and inspection of cranial sutures.

Declaration of Competing Interest

The authors declare that they have no known competing financial interests or personal relationships that could have appeared to influence the work reported in this paper.

Acknowledgments

This work was supported by the National Science Foundation CMMI Award No. 1933158 on Coupling Skull-Brain Vibroacoustics and Ultrasound Toward Enhanced Imaging, Diagnosis, and Therapy.

Appendix A

Following the analysis in [29], the gradient $\nabla_{\mathbf{a}}\mathcal{F}(\mathbf{a}_k)$ and Hessian $\nabla_{\mathbf{a}}^2\mathcal{F}(\mathbf{a}_k)$ in Eq. (4) are expressed as

$$\nabla_{\mathbf{a}}\mathcal{F}(\mathbf{a}_k) = \beta(\|\mathbf{a}_k - \mathbf{a}_{k-1}\|_2^2 + \Delta_{k-1})\mathbf{J}^T(\mathbf{a}_k)\mathbf{r}(\mathbf{a}_k) + \beta\|\mathbf{r}(\mathbf{a}_k)\|_2^2(\mathbf{a}_k - \mathbf{a}_{k-1}), \quad (\text{A.1})$$

$$\begin{aligned} \nabla_{\mathbf{a}}^2\mathcal{F}(\mathbf{a}_k) = & \beta(\|\mathbf{a}_k - \mathbf{a}_{k-1}\|_2^2 + \Delta_{k-1})\mathbf{J}^T(\mathbf{a}_k)\mathbf{J}(\mathbf{a}_k) \\ & + \beta\|\mathbf{r}(\mathbf{a}_k)\|_2^2\mathbf{I} \\ & + 2\beta[\mathbf{J}^T(\mathbf{a}_k)\mathbf{r}(\mathbf{a}_k)] \otimes (\mathbf{a}_k - \mathbf{a}_{k-1}) \\ & + 2\beta(\mathbf{a}_k - \mathbf{a}_{k-1}) \otimes [\mathbf{J}^T(\mathbf{a}_k)\mathbf{r}(\mathbf{a}_k)], \end{aligned} \quad (\text{A.2})$$

in which $\mathbf{r}(\mathbf{a}_k)$ is given in Eq. (6), $\beta = 2/(N_\omega N_a \Delta_{k-1})$, while $\mathbf{J}(\mathbf{a}_k) = [\partial \mathbf{r}(\mathbf{a})/\partial \mathbf{a}]_{\mathbf{a}=\mathbf{a}_k}$ represents the Jacobian of the residual $\mathbf{r}(\mathbf{a}_k)$. The (i,j) -th component of $\mathbf{J}(\mathbf{a}_k)$ corresponds to the derivative of the i -th frequency $\omega_i(\mathbf{a}_k, \kappa)$, $i = 1, \dots, N_\omega$, at a fixed wavenumber κ calculated with respect to the j -th dimensionless parameter $a_{j,j} = 1, \dots, N_a$. Using Eqs. (3) and (6), one obtains

$$[\mathbf{J}(\mathbf{a}_k)]_{ij} = \frac{1}{\tilde{\omega}_i^2(\kappa)} \frac{\mathbf{Q}^H(\mathbf{a}_k)[\mathbf{S}_j(\mathbf{a})]_{\mathbf{a}=\mathbf{a}_k}\mathbf{Q}(\mathbf{a}_k)}{\mathbf{Q}^H(\mathbf{a}_k)\mathbf{M}(\mathbf{a}_k)\mathbf{Q}(\mathbf{a}_k)}, \quad (\text{A.3})$$

in which

$$\mathbf{S}_j(\mathbf{a}) = \frac{\partial(\kappa^2 \mathbf{K}_3(\mathbf{a}) + i\kappa \mathbf{K}_2(\mathbf{a}) + \mathbf{K}_1(\mathbf{a}) - \omega_i^2(k)\mathbf{M}(\mathbf{a}))}{\partial a_j}. \quad (\text{A.4})$$

In the previous equations, the maximum size of the trust region at the k -th iteration is calculated from the quadratic formula

$$\Delta_k = \frac{-d_2 + (d_2^2 - 4d_1d_3)^{1/2}}{2d_1}, \quad (\text{A.5})$$

in which

$$d_1 = N_a^2, \quad (\text{A.6})$$

$$d_2 = 2\text{sgn}(\mathbf{a}_k - \mathbf{a}_{k-1})^T(\mathbf{a}_k - \mathbf{a}_{k-1}), \quad (\text{A.7})$$

$$d_3 = \|\mathbf{a}_k - \mathbf{a}_{k-1}\|_2^2 - 2N_a\Delta_{k-1}, \quad (\text{A.8})$$

where $\text{sgn}(\cdot)$ denotes the signum function. Once Eqs. (A.1)-(A.5) have been evaluated at the k -th iteration, an update $\mathbf{a}_{k+1} = \mathbf{a}_k + \delta\mathbf{a}_k$ can be obtained by calculating $\delta\mathbf{a}_k$ from (4) using the trust region reflective (TRR) method described in [29,35,36].

References

- [1] K. Firouzi, P. Ghanouni, B.T. Khuri-Yakub, Efficient transcranial ultrasound delivery via excitation of lamb waves: Concept and preliminary results, in: 2017 IEEE International Ultrasonics Symposium (IUS), IEEE, 2017, pp. 1–4.
- [2] K. Hynynen, G.T. Clement, N. McDannold, N. Vykhodtseva, R. King, P.J. White, S. Vitek, F.A. Jolesz, 500-element ultrasound phased array system for noninvasive focal surgery of the brain: A preliminary rabbit study with ex vivo human skulls, *Magn. Reson. Med.: An Off. J. Int. Soc. Magn. Reson. Med.* 52 (2004) 100–107.
- [3] J.K. Mueller, L. Ai, P. Bansal, W. Legon, Computational exploration of wave propagation and heating from transcranial focused ultrasound for neuromodulation, *J. Neural Eng.* 13 (2016) 056002, <https://doi.org/10.1088/1741-2560/13/5/056002>.
- [4] A. Hughes, Y. Huang, M.L. Schwartz, K. Hynynen, The reduction in treatment efficiency at high acoustic powers during mr-guided transcranial focused ultrasound thalamotomy for essential tremor, *Med. Phys.* 45 (2018) 2925–2936, <https://doi.org/10.1002/mp.12975>.
- [5] V. Ozenne, C. Constans, P. Bour, M.D. Santin, R. Valabrègue, H. Ahnine, P. Pouget, S. Lehericy, J.-F. Aubry, B. Quesson, Mri monitoring of temperature and displacement for transcranial focus ultrasound applications, *NeuroImage* 204 (2020) 116236, <https://doi.org/10.1016/j.neuroimage.2019.116236>.
- [6] N. McDannold, P.J. White, R. Cosgrove, Predicting bone marrow damage in the skull after clinical transcranial mri-guided focused ultrasound with acoustic and thermal simulations, *IEEE Trans. Med. Imaging* 39 (2020) 3231–3239, <https://doi.org/10.1109/TMI.2020.2989121>.
- [7] L. Deng, A. Hughes, K. Hynynen, A noninvasive ultrasound resonance method for detecting skull induced phase shifts may provide a signal for adaptive focusing, *IEEE Trans. Biomed. Eng.* 67 (2020) 2628–2637, <https://doi.org/10.1109/TBME.2020.2967033>.
- [8] J.D. Achenbach, *Wave Propagation in Elastic Solids*, North-Holland Pub. Co., Amsterdam, 1973.
- [9] M.J.S. lowe, *Plate waves for the NDT of diffusion bonded titanium*, Ph.D. thesis, Imperial College, London, UK, 1992.
- [10] J.L. Rose, *Ultrasonic Waves in Solid Media*, Cambridge University Press, Cambridge, 2004.
- [11] I. Bartoli, A. Marzani, F. Lanza di Scalea, E. Viola, Modeling wave propagation in damped waveguides of arbitrary cross-section, *J. Sound Vib.* 295 (2006) 685–707.
- [12] M. Mazzotti, A. Marzani, I. Bartoli, E. Viola, Guided waves dispersion analysis for prestressed viscoelastic waveguides by means of the safe method, *Int. J. Solids Struct.* 49 (2012) 2359–2372.
- [13] M. Mazzotti, I. Bartoli, A. Marzani, Ultrasonic leaky guided waves in fluid-coupled generic waveguides: hybrid finite-boundary element dispersion analysis and experimental validation, *J. Appl. Phys.* 115 (2014) 1–10.
- [14] N. Bochud, Q. Vallet, J.-G. Minonzio, P. Laugier, Predicting bone strength with ultrasonic guided waves, *Scient. Rep.* 7 (2017), <https://doi.org/10.1038/srep43628>.
- [15] J.-G. Minonzio, N. Bochud, Q. Vallet, Y. Bala, D. Ramiandrisoa, H. Follet, D. Mitton, P. Laugier, Bone cortical thickness and porosity assessment using ultrasound guided waves: An ex vivo validation study, *Bone* 116 (2018) 111–119.
- [16] A.O. Schneider, D. Ramiandrisoa, G. Armbrecht, Z. Ritter, D. Felsenberg, K. Raum, J.-G. Minonzio, In vivo measurements of cortical thickness and porosity at the proximal third of the tibia using guided waves: Comparison with site-matched peripheral quantitative computed tomography and distal high-resolution peripheral quantitative computed tomography, *Ultrason. Med. Biol.* 45 (2019) 1234–1242, <https://doi.org/10.1016/j.ultrasmedbio.2019.01.008>.

- [17] C. Adams, J. McLaughlan, L. Nie, S. Freear, Excitation and acquisition of cranial guided waves using a concave array transducer, in: *Proceedings of Meetings on Acoustics 173EAA*, volume 30, Acoustical Society of America, 2017a, p. 055003.
- [18] C. Adams, J.R. McLaughlan, L. Nie, D. Cowell, T. Carpenter, S. Freear, Excitation of leaky lamb waves in cranial bone using a phased array transducer in a concave therapeutic configuration, *J. Acoust. Soc. Am.* 141 (2017) 3918, <https://doi.org/10.1121/1.4988854>.
- [19] H. Estrada, S. Gottschalk, M. Reiss, V. Neuschmelting, R. Goldbrunner, D. Razansky, Observation of guided acoustic waves in a human skull, *Ultrasound Med. Biol.* 44 (2018) 2388–2392, <https://doi.org/10.1016/j.ultrasmedbio.2018.05.019>.
- [20] H. Estrada, S. Gottschalk, M. Reiss, V. Neuschmelting, J. Rebling, R. Goldbrunner, D. Razansky, Looking at the skull in a new light: Rayleigh-lamb waves in cranial bone, in: *2018 IEEE International Ultrasonics Symposium (IUS)*, 2018, pp. 1–3.
- [21] J. Gao, Q. Chen, C. Jiang, B. Hu, J. Zhang, K. Xu, D. Ta, A free plate model could predict ultrasonic guided waves propagation in a 3d printed skull phantom, in: *2019 IEEE International Ultrasonics Symposium (IUS)*, 2019, pp. 2031–2033.
- [22] H. Estrada, J. Rebling, D. Razansky, Prediction and near-field observation of skull-guided acoustic waves, *Phys. Med. Biol.* 62 (2017) 4728–4740, <https://doi.org/10.1088/1361-6560/aa63e3>.
- [23] H. Estrada, J. Rebling, D. Razansky, Observation of skull-guided acoustic waves in a water-immersed murine skull using optoacoustic excitation, in: K.V. Larin, D. Sampson (Eds.), *Optical Elastography and Tissue Biomechanics IV*, volume 10067, International Society for Optics and Photonics, SPIE, 2017, pp. 62–65, <https://doi.org/10.1117/12.2252089>.
- [24] Y. Hua, T.K. Sarkar, Matrix pencil method for estimating parameters of exponentially damped/undamped sinusoids in noise, *IEEE Trans. Acoust. Speech Signal Process.* 38 (1990) 814–824, <https://doi.org/10.1109/29.56027>.
- [25] M. Ekstrom, Dispersion estimation from borehole acoustic arrays using a modified matrix pencil algorithm, in: *Signals, Systems and Computers*, 1995. 1995 Conference Record of the Twenty-Ninth Asilomar Conference on, volume 1, 1995, pp. 449–453.
- [26] M. Mazzotti, I. Bartoli, G. Castellazzi, A. Marzani, Computation of leaky guided waves dispersion spectrum using vibroacoustic analyses and the matrix pencil method: A validation study for immersed rectangular waveguides, *Ultrasonics* 54 (2014) 1895–1898, <https://doi.org/10.1016/j.ultras.2014.05.009>.
- [27] G. Golub, C.V. Loan, *Matrix Computations*, second ed., Johns Hopkins Press, Baltimore, MD, 1989.
- [28] J. Peterson, P.C. Dechow, Material properties of the human cranial vault and zygoma, *Anatom. Rec. Part A: Discove. Mol., Cell., Evol. Biol.* 274A (2003) 785–797, <https://doi.org/10.1002/ar.a.10096>.
- [29] M. Mazzotti, Q. Mao, I. Bartoli, S. Livadiotis, A multiplicative regularized gauss-newton method with trust region sequential quadratic programming for structural model updating, *Mech. Syst. Signal Process.* 131 (2019) 417–433, <https://doi.org/10.1016/j.ymsp.2019.05.062>.
- [30] M. Culjat, D. Goldenberg, P. Tewari, R. Singh, Material review of tissue substitutes for ultrasound imaging, *Ultrasound Med. Biol.* 36 (2010) 861–873, <https://doi.org/10.1016/j.ultrasmedbio.2010.02.012>.
- [31] F. Evans, H. Lissner, Tensile and compressive strength of human parietal bone, *J. Appl. Physiol.* 10 (1957) 493–497, <https://doi.org/10.1152/jappl.1957.10.3.493>.
- [32] F. Linde, I. Hvid, The effect of constraint on the mechanical behaviour of trabecular bone specimens, *J. Biomech.* 22 (1989) 485–490, [https://doi.org/10.1016/0021-9290\(89\)90209-1](https://doi.org/10.1016/0021-9290(89)90209-1).
- [33] S. Boruah, K. Henderson, D. Subit, R.S. Salzar, B.S. Shender, G.R. Paskoff, Response of human skull bone to dynamic compressive loading, in: *International Research Council on the Biomechanics of Injury (IRCOBI)*, Gothenburg, Sweden, 2013, pp. 497–508.
- [34] T.N. Tran, L. Stieglitz, Y.J. Gu, L.H. Le, Analysis of ultrasonic waves propagating in a bone plate over a water half-space with and without overlying soft tissue, *Ultrasound Med. Biol.* 39 (2013) 2422–2430.
- [35] T. Coleman, Y. Li, An interior trust region approach for nonlinear minimization subject to bounds, *SIAM J. Optim.* 6 (1996) 418–445, <https://doi.org/10.1137/0806023>.
- [36] M. Branch, T. Coleman, Y. Li, A subspace, interior, and conjugate gradient method for large-scale bound-constrained minimization problems, *SIAM J. Scient. Comput.* 21 (1999) 1–23, <https://doi.org/10.1137/S1064827595289108>.